Author/s:
Bhangu, SK;Charchar, P;Noble, BB;Kim, C-J;Pan, S;Yarovsky, I;Cavalieri, F;Caruso, F

Title:
Origins of Structural Elasticity in Metal-Phenolic Networks Probed by Super-Resolution Microscopy and Multiscale Simulations.

Date:
2022

Citation:
Bhangu, S. K., Charchar, P., Noble, B. B., Kim, C. -J., Pan, S., Yarovsky, I., Cavalieri, F. & Caruso, F. (2022). Origins of Structural Elasticity in Metal-Phenolic Networks Probed by Super-Resolution Microscopy and Multiscale Simulations.. ACS Nano, 16 (1), pp.98-110. https://doi.org/10.1021/acsnano.1c08192.

Persistent Link:
https://hdl.handle.net/11343/297205

On the Origins of Structural Elasticity in Metal–Phenolic Networks Probed by Super-Resolution Microscopy and Multiscale Simulations

Sukhvir Kaur Bhangu,[1,2,‡] *Patrick Charchar,*[3,‡] *Benjamin Noble,*[3] *Chan-Jin Kim,*[1] *Shuaijun Pan,*[1] *Irene Yarovsky,*[3]* *Francesca Cavalieri,*[2,4]* *and Frank Caruso*[1]*

[1]ARC Centre of Excellence in Convergent Bio-Nano Science and Technology, and the Department of Chemical Engineering, The University of Melbourne, Parkville, Victoria 3010, Australia

[2]School of Science, RMIT University, Victoria 3001, Australia

[3]School of Engineering, RMIT University, Victoria, 3001, Australia

[4]Dipartimento di Scienze e Tecnologie Chimiche, Università degli Studi di Roma "Tor Vergata", via della ricerca scientifica 1, 00133, Rome, Italy

*Corresponding authors. Email: irene.yarovsky@rmit.edu.au (I. Y.); francesca.cavalieri@rmit.edu.au (F. Cavalieri); fcaruso@unimelb.edu.au (F. Caruso)

ABSTRACT

Metal–phenolic networks (MPNs) are amorphous materials that can be used to engineer functional films and particles. A fundamental understanding of the heat-driven structural reorganization of MPNs can offer opportunities to rationally tune their properties (*e.g.*, size, permeability, wettability, hydrophobicity) for applications such as drug delivery, sensing, and tissue engineering. Herein, we use a combination of single-molecule localization microscopy, theoretical electronic structure calculations, and all-atom molecular dynamics simulations to demonstrate that MPN plasticity is governed by both the inherent flexibility of the metal (Fe^{III})–phenolic coordination center and the conformational elasticity of the phenolic building blocks (tannic acid, TA) that make up the metal–organic coordination complex. Thermal treatment (heating to 150 °C) of the flexible TA/Fe^{III} networks induces a considerable increase in the number of aromatic π–π interactions formed among TA moieties and leads to the formation of hydrophobic domains. In the case of MPN capsules, 15 min of heating induces structural rearrangements that cause the capsules to shrink (from ~4 to ~3 μm), resulting in a thicker (3-fold), less porous, and more adhesive MPN shell. In contrast, when a simple polyphenol such as gallic acid is complexed with Fe^{III} to form MPNs, rigid materials that are insensitive to temperature changes are obtained, and negligible structural rearrangement is observed upon heating. These findings are expected to facilitate the rational engineering of versatile TA-based MPN materials with tunable physiochemical properties for diverse applications.

KEYWORDS: metal–phenolic networks, structural reorganization, super-resolution microscopy, PAINT, molecular dynamics

Thin layer coatings and hydrogels based on metal–phenolic networks (MPNs) have attracted attention due to their potential application in drug delivery, catalysis, environmental remediation, and forensics.[1,2] The formation of MPNs is primarily controlled by the rapid complexation between metal ions (*e.g.*, Fe^{III}) and the catechol moieties present in polyphenol molecules. The catechol–Fe^{III} coordination bonds have stability comparable to that of a covalent bond.[3] A range of metal ions and ligands can be used to form nanostructured MPN films and particles/capsules within minutes.[2,4] Numerous methods have been presented for the synthesis of MPN coatings and capsules *e.g.*, discrete assembly, rust-mediated continuous assembly, and oxidative-mediated continuous assembly.[5–7] The mechanical properties and the stability of MPN films have been tuned by controlling different parameters including the type of the phenolic building block, metal-to-catechol ratio, mixing time, pH, and ionic strength.[4,8–10] Recently, we reported the transformation of MPN capsules *via* pyrolysis and combustion at 773 K into metal–carbon network and metal oxide network capsules, respectively.[11] However, heat-induced structural changes of MPN materials at temperatures that do not cause chemical transformation of the materials (*e.g.*, up to the glass transition temperature (T_g)) remain unexplored. Herein, we examine how thermally induced structural rearrangements of MPN capsules and films enable fine-tuning of their functional properties (*i.e.*, permeability, hydrophobicity, wettability, protein adsorption), providing structure–property insights that are advantageous for developing MPN materials for potential applications in the fields of drug delivery, tissue engineering, sensing, and membrane separation.[12]

A number of studies were conducted to explore thermal effects on thin films, including multilayered polyelectrolyte films assembled by layer-by-layer techniques.[13,14] After thermal treatment above T_g, the multilayered polyelectrolyte microcapsules exhibited changes in size, morphology, and permeability.[13,15] Heating induced the transient dissociation of ion pairs and enabled the polyelectrolyte chains to rearrange into coiled conformations that were more energetically favored.[15,16] This rearrangement was likely driven by an increase in both the entropy of the coiled/entangled polymer chains and the number of hydrophobic interactions between the hydrocarbon chains relative to the ordered and low entropy multilayer states. MPNs specifically based on tannic acid (TA), in some ways, resemble polyelectrolyte networks and exhibit similar characteristics. In particular, the supramolecular assembly of TA/$\mathrm{Fe}^{\mathrm{III}}$ or gallic acid (GA)/$\mathrm{Fe}^{\mathrm{III}}$ MPNs is regulated by coordination bonds between the metal ions and galloyl moieties at room temperature (**Figure 1a**), thereby leading to kinetically trapped structures.[7,17,18] In addition, hydrogen bonding between OH groups and hydrophobic (p–π and π–π) interactions between galloyl moieties can contribute to the stabilization of the networks.[19] However, at elevated temperatures this interplay of intermolecular interactions may be disrupted to trigger structural changes in the network, similar to the rearrangements observed for the coordination between phenylene tetra-carboxylate and metal ions in going from ambient to elevated temperatures.[20]

In the present study, we investigate the structural reorganization and related property changes of two metal-coordinated polyphenol networks following thermal treatment (150 °C), namely TA/$\mathrm{Fe}^{\mathrm{III}}$ and GA/$\mathrm{Fe}^{\mathrm{III}}$ MPNs in the form of thin films and microcapsules. Specifically, we elucidate how thermal treatment up to T_g influences the morphology, thickness, roughness, permeability, and hydrophobicity of the MPN films and capsules. Our study shows that the heat-driven structural rearrangements of the amorphous and flexible TA/$\mathrm{Fe}^{\mathrm{III}}$ MPNs are associated with the formation of hydrophobic domains inside the network. To monitor MPN rearrangements at the molecular level upon heating, we employ a super-resolution microscopy technique, *i.e.*, points accumulation for imaging in nanoscale topography (PAINT).[21,22] Using a phenoxazine-based dye (Nile Red, NR)[23] that is sensitive to hydrophobic environments,[24–26] we probe and quantify the formation of hydrophobic nanodomains within the MPN capsules and films. In contrast, GA/Fe^{III} MPNs appeared as rigid materials that are insensitive to temperature changes and have limited capacity to structurally rearrange upon heating. Furthermore, theoretical electronic structure calculations and all-atom molecular dynamics (MD) simulations reveal that structural rearrangement of MPNs is modulated by the inherent elasticity of the Fe^{III}–phenol coordination center and the conformational flexibility of the constituent phenolic building blocks. This work provides molecular insights into the mechanisms that govern the structural changes of MPNs due to thermal treatment and offers opportunities for the rational manipulation of the structural properties of metal–organic coordination networks.

Results and Discussions

Synthesis and Thermal Treatment of MPN Capsules. MPN films and capsules were prepared using the discrete assembly method.[4] Briefly, by mixing a suspension of polystyrene (PS) microparticles with $FeCl_3$ (15 mM) and TA (10 mM) aqueous solutions, a TA/Fe^{III} network coating immediately formed on the PS particles. MPN capsules were obtained following dissolution of the PS templates. A schematic of the assembly process is depicted in **Figure 1a**. Uniformly spherical TA/Fe^{III} capsules, 3.8 ± 0.4 µm in diameter, were obtained, as shown in the optical microscopy (**Figure 1b**) and scanning electron microscopy (SEM) (**Figures 1c** and **S1**) images. The bilayer thickness of the TA/Fe^{III} capsules was 28 ± 4 nm, as determined from atomic force microscopy (AFM) images, corresponding to a single layer thickness of ~14 nm (**Figures S2** and **S3**). The capsules exhibited a characteristic ligand-to-metal charge transfer band at ~585 nm (**Figure S4**) and an iron peak from the energy-dispersive X-ray spectroscopy (EDS) analysis (**Figure S5**) owing to the formation of TA/Fe^{III} complexes. The number of iron atoms coordinated to a single TA molecule was ~3, as determined by inductively coupled plasma–optical emission spectroscopy (ICP-OES). The red shift of the C–O stretching bands at 1171 and 1307 cm^{-1} to 1188 and 1316 cm^{-1}, respectively, in the Fourier-transform infrared (FTIR) spectrum (**Figure S6**) of the TA/Fe^{III} MPN capsules (air-dried) indicates coordination of the galloyl groups to the metal ions. In addition, the peaks at 1533 and 1443 cm^{-1} in the TA spectrum, which were attributed to C–C stretching vibration in the aromatic rings, shifted to 1573 and 1432 cm^{-1}, respectively, in the FTIR spectrum of TA/Fe^{III} MPN capsules, confirming the presence of intermolecular π–π stacking interactions in the MPN capsules.

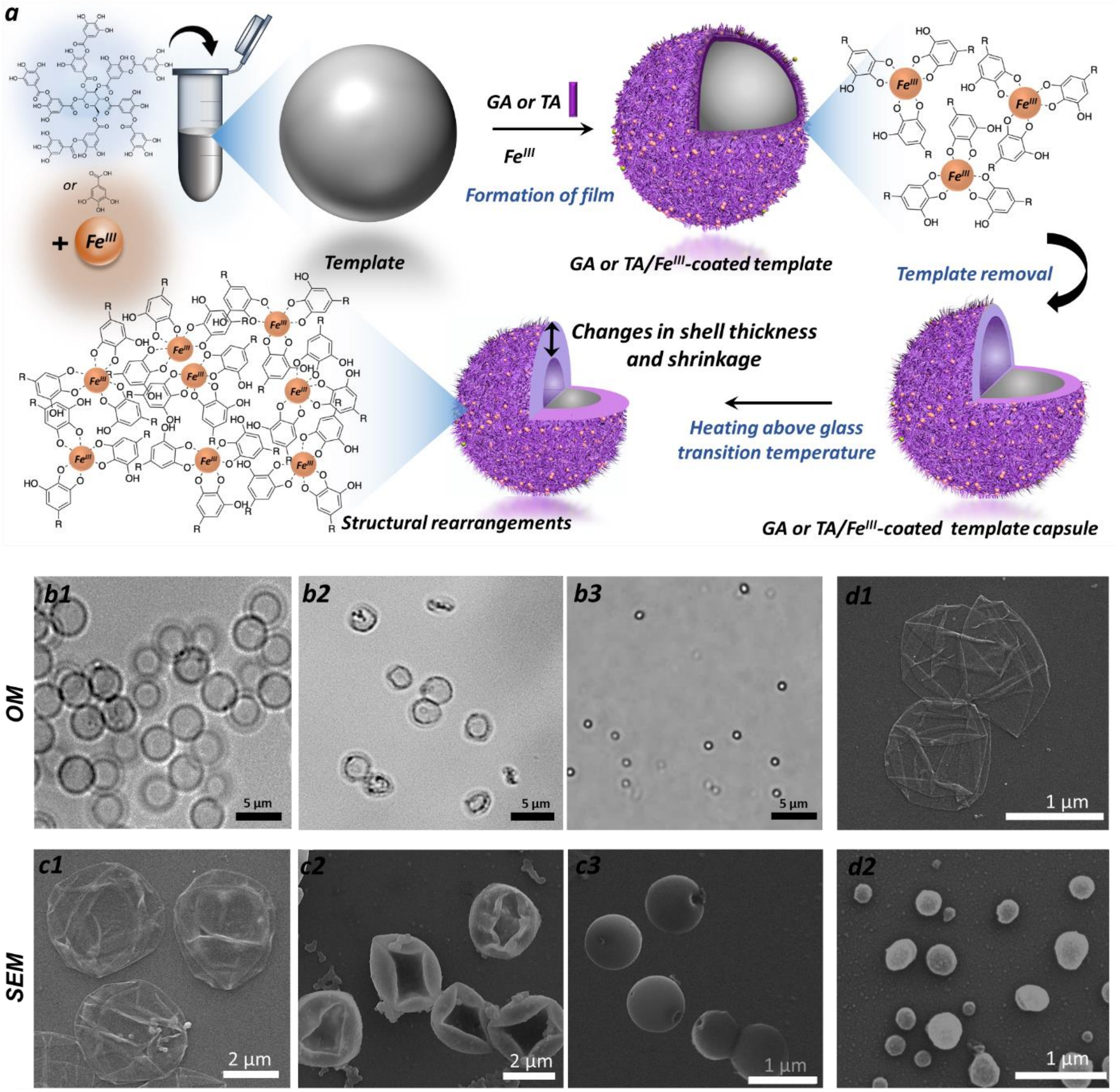

Figure 1. Effect of temperature on the morphology and rearrangement of MPN capsules. (a) Schematic illustrating the template-mediated, coordination-driven assembly of GA/Fe^{III} or TA/Fe^{III} capsules, and structural changes occurring in the TA/Fe^{III} capsules upon heating at 150 °C for 15 min. (b) Optical microscopy (OM) and (c) SEM images of TA/Fe^{III} capsules before heat treatment (b1, c1), and after heat treatment for 15 min at 150 °C (b2, c2) or 30 min at 150 °C (b3, c3); the capsules were prepared using 3 μm PS templates. (d) SEM images of TA/Fe^{III} capsules

before heating (d1) and after heating at 150 °C for 30 min (d2); the capsules were prepared using 1 μm PS templates.

To investigate the possible effect of temperature on the morphology and rearrangement of the MPN capsules, the T_g values of TA and the TA/Fe^{III} network were determined; these were around 93 °C (**Figure S7**) and around 109 °C (**Figure S8**), respectively. This suggests that the amorphous MPN network is organized in a rigid structure at the lower temperature range, whereas network conformational mobility is enhanced when heated up to the T_g.

The effect of thermal treatment on the morphology and structure of the TA/Fe^{III} capsules was studied by heating a TA/Fe^{III} capsule suspension at 150 °C for 15 or 30 min and subsequently analyzing the air-dried capsules. For comparison, an aqueous suspension of TA/Fe^{III} capsules was also treated in an autoclave at 120 °C for 20 min and then analyzed. Optical microscopy (**Figure 1b**) and SEM (**Figures 1c and S9**) images show that the microcapsules maintained their integrity after both types of thermal treatment but a significant size reduction and change in morphology occurred. We did not observe differences in the morphology of the capsules for the two thermal treatments employed. After heat treatment at 150 °C for 15 and 30 min, the size of the capsules decreased from 3.8 ± 0.4 μm (**Figure 1b1, 1c1**) to 2.9 ± 0.3 μm (**Figures 1b2, 1c2 and S9a**) and 1.1 ± 0.1 μm (**Figure 1b3, 1c3**), respectively.

The AFM images (**Figures S2 and S10**) of the TA/Fe^{III} capsules suggest that the capsule shrinkage observed is in accordance with an increase in shell thickness. The bilayer thickness of the heat-treated capsules determined from the AFM images was ~90 nm on average, which is >3-fold thicker than the bilayer thickness of the capsules before heat treatment (**Figure S3**). Similarly, TA/Fe^{III} capsules prepared using smaller sacrificial PS templates (1 μm), where the capsules shrank from 1.3 μm (**Figure 1d1**) to 0.4 μm following thermal treatment at 150 °C for 30 min

(**Figure 1d2**). The stiffness values of the hydrated capsules before and after heat treatment were evaluated by AFM force measurements. **Figure 2a** and **Figure 2b** respectively compare the force–deformation (*F*–*δ*) curves and stiffness values of the TA/Fe^{III} capsules before and after heat treatment (15 min, 150 °C). The stiffness values, determined from the slope of the curves,[7] were 34 ± 8 and 68 ± 22 mN m^{-1} for the TA/Fe^{III} capsules before and after heat treatment, respectively (**Figure 2b**). The increase in the stiffness of the capsules after heat treatment is attributed to the larger wall thickness of the heat-treated capsules (~14 nm *vs* ~90 nm).

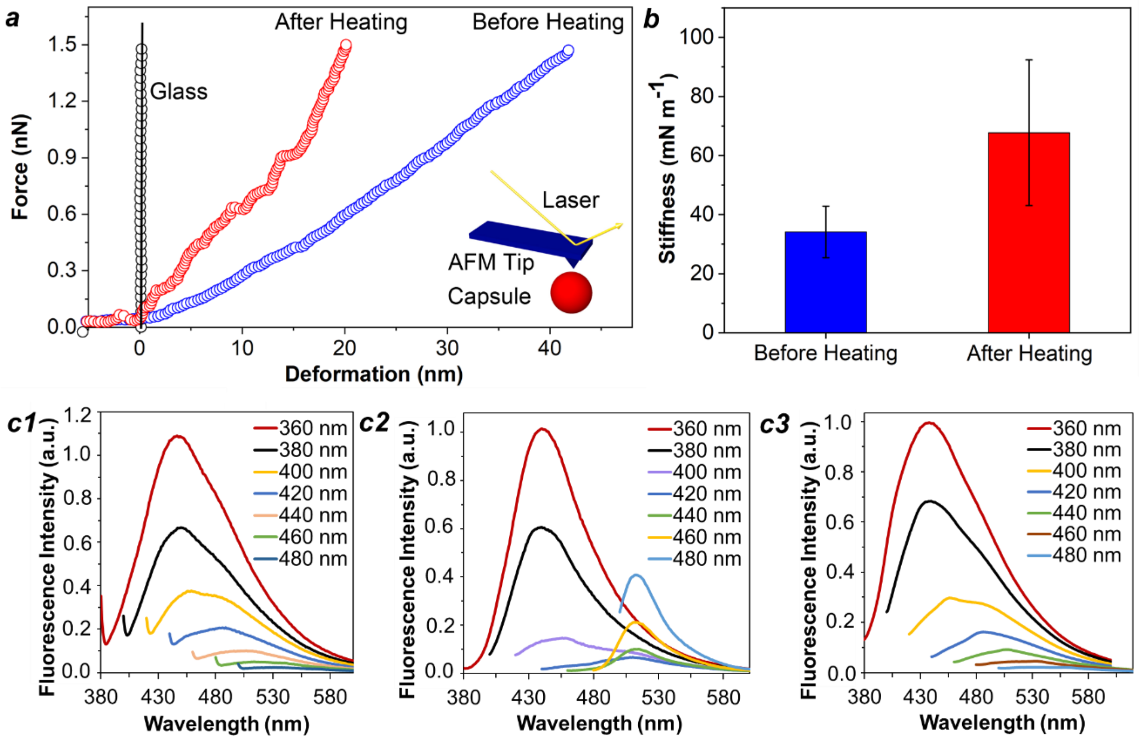

Figure 2. (a, b) Representative force–deformation (*F*–*δ*) curves (a) and corresponding stiffness profiles (b) of the TA/Fe^{III} capsules before and after heat treatment at 150 °C for 15 min. The *F*–*δ* curve of a glass substrate is also shown for comparison. The data are shown as mean stiffness ± standard deviation ($n = 5$). (c) Fluorescence emission spectra of TA/Fe^{III} capsule suspensions in water measured at different excitation wavelengths: before heat treatment (c1); after heat treatment at 150 °C for 15 min (c2); and after heat treatment at 150 °C for 15 min and subsequent addition of dimethyl sulfoxide (c3).

Note that the emission band at ~520 nm (excitation at 480 nm) emerges after heat treatment (c2) but disappears upon subsequent addition of dimethyl sulfoxide (c3).

To gain insight into the mechanism underlying the heat-induced rearrangements of the MPN networks, we explored whether thermal treatment causes the degradation of TA or the disassembly of TA/Fe^{III} complexes. TA was subjected to the thermal treatment studied herein and thereafter analyzed by high-performance liquid chromatography (HPLC). The HPLC results suggest that TA (peak at retention time of 16.4 min) degrades into GA (peak at retention time of 8.4 min) and other low molecular weight products (eluting within a retention time range of 13–16 min), as determined from increases in their HPLC peak intensities after thermal treatment (**Figure S11**). In contrast, TA degradation was negligible in the TA/Fe^{III} complexes heat-treated to 150 °C (**Figure S12**). In addition, HPLC analysis of the heat-treated TA/Fe^{III} complexes indicates that the formation of higher molecular weight species, arising from thermally induced TA polymerization in the TA/Fe^{III} complexes, can be ruled out, as such species would be expected to elute after TA.

This observation indicates that the complexation of TA with Fe^{III} imparts stability to the phenolic molecules against thermal decomposition, which is also confirmed by thermogravimetric analysis (TGA) performed in the temperature range of 25–900 °C. The thermogram of the TA/Fe^{III} capsules (**Figure S13**) shows that heating the air-dried capsules up to 150 °C was accompanied by expulsion of water molecules entrapped within the network and heating above 300 °C resulted in the slow degradation of the complexes. In contrast, ~60% of uncoordinated TA degraded at temperatures around 300 °C. Furthermore, no evidence of TA degradation or complex disassembly was found by HPLC analysis (**Figure S14**) following heating and resuspension of the capsules.

Overall, these results indicate that the TA/Fe^{III} capsules are responsive to changes in temperature, displaying heat-induced shrinking behaviors, and consequently leading to smaller and thicker MPN capsules. Our findings reveal that capsule shrinkage is not due to thermal degradation or disassembly of TA/Fe^{III} complexes but rather is likely caused by structural rearrangements within the network (discussed later in further detail). We expect that changes in hydrogen bonding, π–π interactions, ligand–metal electrostatic interactions, and water coordination lead to the observed structural rearrangement of the network when the TA/Fe^{III} capsules are heated around the T_g. In the high-temperature regime (>110 °C), the breakage of H-bonding interactions and the rotation of the galloyl units of the branched TA may cause defects in the MPNs. These defects in the network can be restored to form a more compact network upon cooling and resuspension of the capsules in water.

We hypothesize that the structural rearrangement of the TA/Fe^{III} network is primarily driven by an increase in π–π interactions among the multiple aromatic groups present in TA, as the strength of hydrophobic interactions typically increases with an increase in temperature.[27] This is supported by the fluorescence emission spectra of the untreated and heat-treated TA/Fe^{III} capsules. Unlike TA, which typically shows a very weak fluorescence signal at 400 nm (**Figure S15**), the untreated MPN capsules showed an intense emission band at 450 nm (**Figure 2c1**), suggesting that the coordination of TA to Fe^{III} ions induces an increase in fluorescence, similar to that observed in flavonoid–metal coordination complexes.[28] A spectral red shift of the fluorescence band was also observed when the excitation wavelength was changed from 360 to 460 nm (**Figure 2c1**). The shift in the emission maximum can be ascribed to the intermolecular association of galloyl moieties *via* hydrogen bonding and/or π–π stacking interactions within the MPN network. The heat-treated TA/Fe^{III} capsules showed an additional band at 520 nm when the capsules were excited at 480 nm (**Figure 2c2**). The appearance of this additional band is likely due to a higher electron delocalization in the network, enabled by π–π intermolecular interactions. The disappearance of that band following suspension of the capsules in dimethyl sulfoxide (to break such interactions) confirms our hypothesis that intra and/or intermolecular π–π interactions are formed at elevated temperatures (**Figure 2c3**).

PAINT-Based Hydrophobicity Tracking of MPN Capsules and Films. To probe the hydrophobicity of the TA/Fe^{III} network and heat-driven rearrangements of TA/Fe^{III} at the molecular level, a single-molecule localization microscopy technique was used. Mapping and imaging of the hydrophobic domains in the network with nanometer resolution was achieved by using the PAINT technique and the dye NR. The bound dye molecules can either dissociate or photobleach, allowing other molecules to bind to the hydrophobic domains. Binding of the probe to hydrophobic regions occurs on a transient timescale, resulting in blinking events that can be recorded for the localization of single molecules and the reconstruction of super-resolution images.[22] PAINT was used to image and quantify the number of hydrophobic sites in the TA/Fe^{III} capsules before and after thermal treatment. Representative PAINT microscopy images of TA/Fe^{III} capsules before and after thermal treatment for 15 min at 150 °C (**Figures 3a, 3b** and **S16**) show the localization of single NR molecules, reflecting the distribution of hydrophobic binding sites on the capsules. From the magnified image in **Figure 3b2**, it is observed that heating significantly increased the density of capsule-bound NR molecules when compared with the untreated capsules (**Figure 3b1**). The heatmaps of selected regions in **Figure 3a1** and **3a2** qualitatively correlate the increase in signal density to an enhanced clustering of NR molecules bound to the heat-treated capsules (**Figure 3c1** and **3c2**). The number of bound NR molecules was quantified *via* intensity-based counting[29] and an automatic count from the Nikon NIS elements software. Overall, the spatial mapping of the capsules using PAINT provides direct evidence that the heat-driven rearrangement of TA/Fe^{III} networks minimizes the energy and entropy of the material *via* the formation of hydrophobic domains that are stabilized by π–π intermolecular interactions. The proposed mechanism is schematically depicted in **Figure 1a**. From the analysis of >20 capsules subjected to each thermal treatment, the number of bound NR molecules increased from ~100 molecules/μm^2 (untreated capsules) to ~800 molecules/μm^2 (heat-treated capsules for 15 min, **Figure 3d**). The protein albumin is known to bind to several hydrophobic drugs;[30] hence, the large number of surface-exposed hydrophobic sites observed after heat treatment was also supported by an enhancement in the adsorption of protein molecules (albumin–fluorescein isothiocyanate (FITC), **Figure 3e**) onto the heat-treated capsules, as observed in the single-molecule localization microscopy images in **Figure 3f** of the protein-adsorbed MPN capsules.

The change in morphology of the heat-treated TA/Fe^{III} capsules led to a decrease in their permeability owing to the shrinkage and increased bilayer thickness, as shown by the reduced permeation of FITC-dextran (20 kDa) into the heat-treated capsules (**Figure S17**) relative to the untreated capsules. Hence, we envisage that heat-driven MPN rearrangements can potentially be exploited to facilitate the engineering of capsules with tunable morphology, thickness, permeability, and surface properties, which in turn can be tailored to improve the loading of hydrophobic drugs.

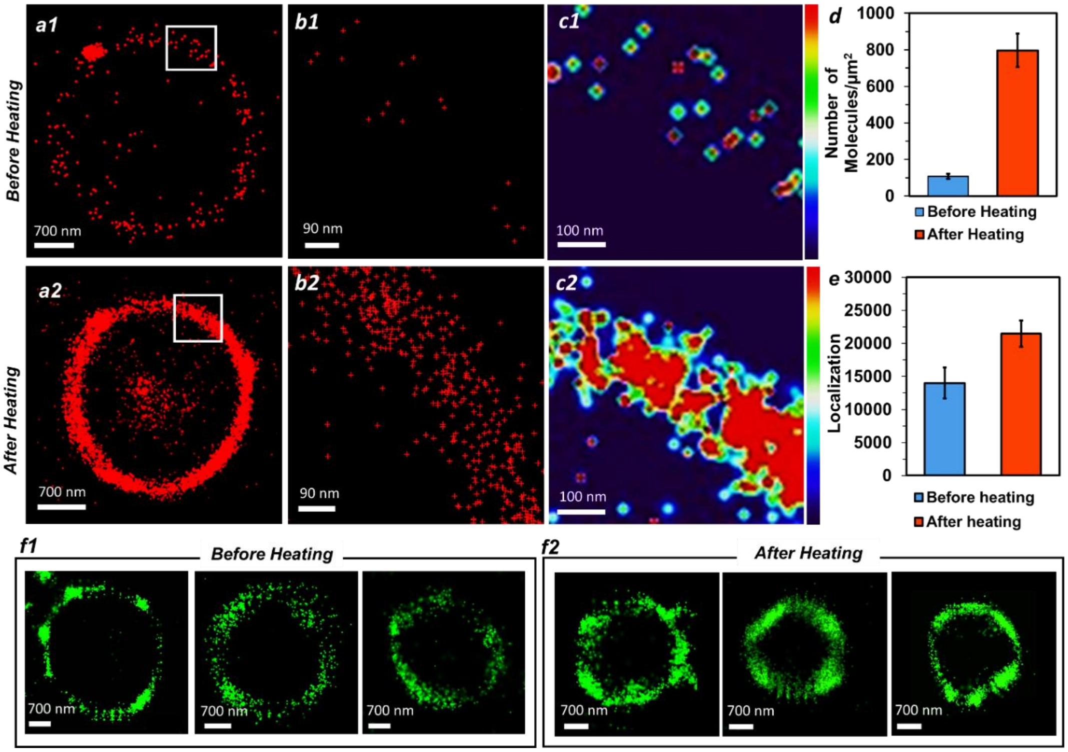

Figure 3. (a, b) PAINT images (a total of 6000 frames with an exposure time of 40 ms were collected) of TA/Fe^{III} capsules at two different resolutions, showing the distribution of hydrophobic sites on the capsules before (a1, b1) and after (a2, b2) heat treatment at 150 °C for 15 min. (c) Heatmaps of the white-boxed regions shown in (a1) and (a2) to illustrate the density and clustering of the NR probe in hydrophobic domains of the TA/Fe^{III} capsules. Color is used to indicate the molecular density/degree of clustering from low (violet) to high (red). (d) Comparison of the number hydrophobic sites identified in the TA/Fe^{III} capsules before and after heating; the capsules were synthesized using the discrete assembly method. (e) Localization profiles comparing the number of albumin–FITC molecules binding to TA/Fe^{III} capsules before and after heating at 150 °C for 15 min. (f) Super-resolution microscopy images showing albumin–FITC molecules bound to the TA/Fe^{III} capsules before (f1) and after (f2) heating.

We postulate that the branched structure of TA plays a key role in imparting malleability to the MPN network, enabling molecular rearrangement at temperatures around and above the T_g. To demonstrate our hypothesis, GA/Fe^{III} MPN capsules were prepared. MPN networks constructed from Fe^{III} and low molecular weight phenolic molecules, such as GA, are known to be stiffer than MPN networks prepared from TA/Fe^{III}; for example, GA/Fe^{III} capsules have a Young's modulus twice that of TA/Fe^{III} capsules.[10] This suggests that the GA/Fe^{III} coordination complex likely lacks the required conformational freedom to undergo structural reorganization under thermal treatment. The presence and complexation of Fe^{III} in the prepared GA/Fe^{III} capsules was confirmed from EDS mapping analysis (**Figure S18a**). The T_g of GA/Fe^{III} complex (~105 °C) (**Figure S18b**) was comparable to that of TA/Fe^{III} (~109 °C). However, compared to the TA/Fe^{III} network (Figure S8), the change in heat capacity of GA/Fe^{III} was hardly noticeable indicating that a limited glass transition occurred in the network.

Comparison of the GA/Fe^{III} capsules before (**Figure 4a1**) and after (**Figure 4a2**) heating to 150 °C for 15 min revealed no apparent changes in the morphology or size of the capsules. PAINT imaging (**Figures 4b1**, **4b2** and **S19**) and heatmaps (**Figure 4c1** and **4c2**) show that the GA/Fe^{III} capsules do not undergo significant rearrangement upon heating, as the number of molecules per square micrometer bound to hydrophobic domains only slightly increased from ~215 to ~250 (**Figure 4d**). Additionally, no significant changes in the fluorescence emission profile of the GA/Fe^{III} capsules after thermal treatment (**Figure 4e2**) were observed (relative to that of the untreated GA/Fe^{III} capsules). Furthermore, a fluorescence band at 520 nm, which was previously ascribed to the formation of hydrophobic domains after thermal treatment, was absent in the profile of the heat-treated GA/Fe^{III} capsules. Collectively, the data suggest that the heat-induced molecular reorganization of MPN networks and associated changes in capsule morphology, size, and thickness are dictated by the conformational flexibility of the phenolic moiety involved in the metal–organic coordination complex.

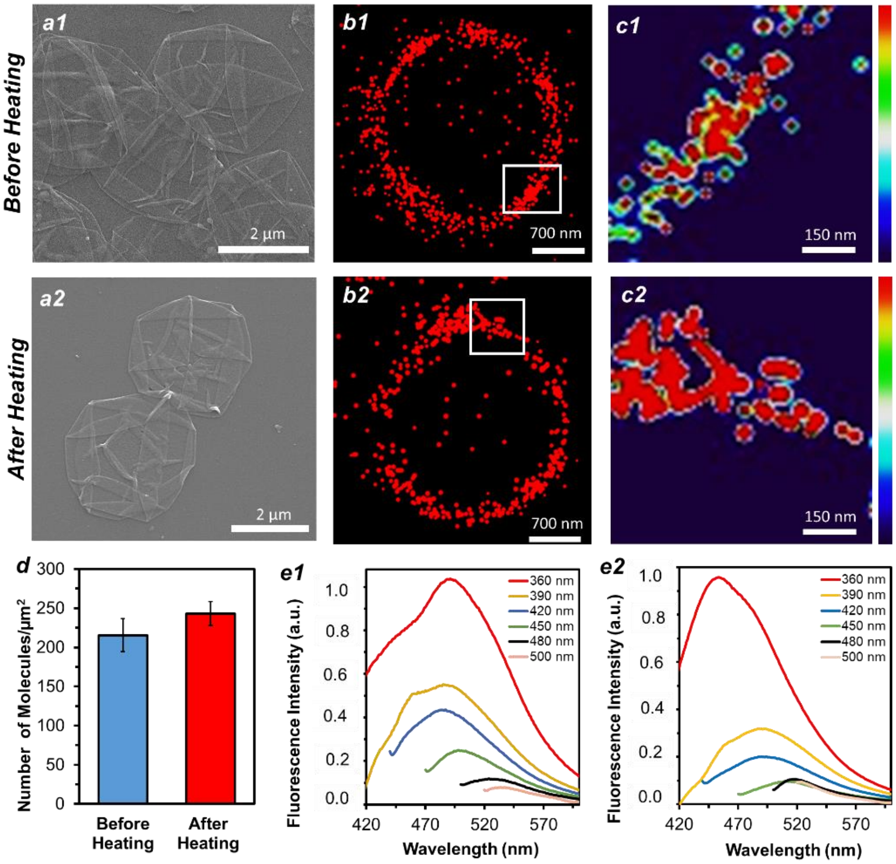

Figure 4. (a) SEM images of GA/Fe^{III} capsules before heat treatment (a1) and after heating at 150 °C for 15 min (a2). (b) PAINT images of GA/Fe^{III} capsules before heat treatment (b1) and after heating at 150 °C for 15 min (b2). (c) Heatmaps of the white boxed regions in (b1) and (b2) illustrating the density and clustering of the NR probe in hydrophobic domains of the GA/Fe^{III} capsules. Color is used to indicate the molecular density/degree of clustering from low (violet) to high (red). (d) Quantitative comparison of the number of hydrophobic sites identified in the GA/Fe^{III} capsules before and after heating. (e) Fluorescence emission spectra of the GA/Fe^{III} capsules at different excitation wavelengths before (e1) and after (e2) heating.

Given the sensitivity of PAINT imaging in probing structural rearrangements of MPNs and the presence of hydrophobic domains in the capsule shell, we examined the applicability of our approach to planar MPN coatings (*i.e.*, films). TA/Fe^{III} coatings (**Figure S20**) were prepared by the deposition of an MPN film on a glass substrate, as confirmed by AFM (**Figure 5a**) and EDS mapping (**Figure S21**). The glass slide with the coated film was incubated at 150 °C for 1 h. The AFM images of the untreated (**Figure 5a1**) and heat-treated (**Figure 5a2**) films indicate that the root-mean-square film roughness decreased from ~5 to ~3 nm after heating. The PAINT images of the TA/Fe^{III} coatings in **Figures 5b**–**5e** and **S22** show mapping of the localization of single NR probe molecules before and after thermal treatment. As observed from **Figure 5b2** and **5c2**, heat treatment enhanced the clustering of NR molecules on the TA/Fe^{III} film, corresponding to the formation of hydrophobic domains. Comparison of the magnified images of the hydrophobic domains observed before and after thermal treatment (**Figures 5d1, S23** and **Figures 5d2, S24**) also indicates that the mean hydrophobic domain size increased from ~100 to ~225 nm after heating. The size distributions of TA/Fe^{III} clusters in the films before and after thermal treatment are shown in **Figure 5f1** and **5f2**. Image analysis reveals a 10–15-fold increase in the density of TA/Fe^{III} molecules (**Figure S25a**) and a ~5-fold increase in the number of TA/Fe^{III} clusters (**Figure S25b**) in the heat-treated film coated on a glass slide compared to the untreated film. The number of detected molecules per hydrophobic cluster also increased from ~25 to ~220 (**Figures 5g1** and **5g2** and **S25c**). The higher hydrophobicity of the heat-treated film was also confirmed by surface wettability measurements, where the contact angle of the TA/Fe^{III} films increased from 22.9° ± 3.5° to 30.2° ± 4.4° after heating.

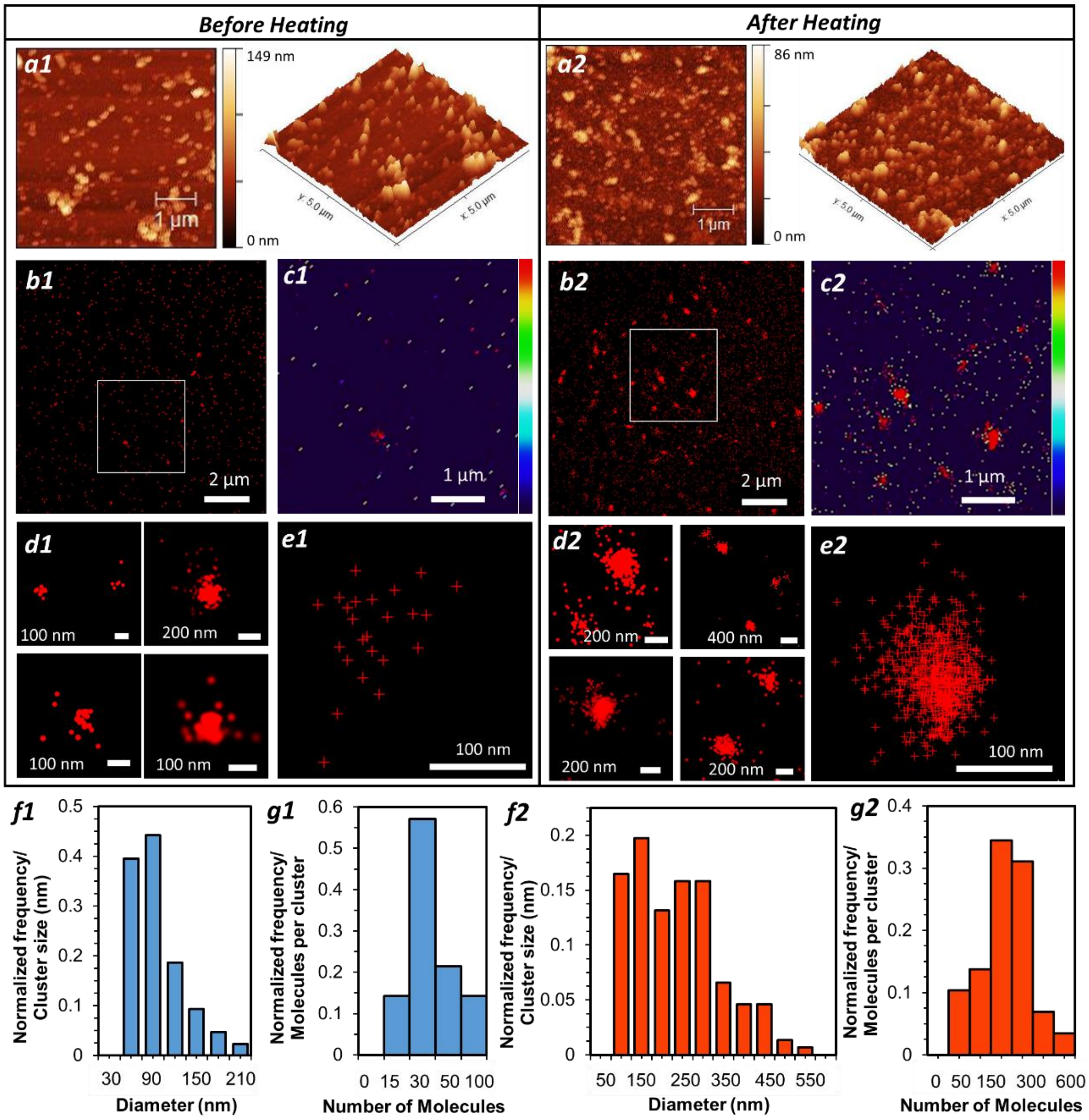

Figure 5. (a) AFM images of the TA/Fe^{III} films before (a1) and after (a2) heating at 150 °C for 1 h. (b) PAINT images showing the hydrophobicity mapping of the TA/Fe^{III} films before (b1) and after (b2) heat treatment at 150 °C for 1 h. (c) Heatmaps of the white boxed regions shown in (b1) and (b2) illustrating the density and clustering of the NR probe in the hydrophobic domains of the TA/Fe^{III} films. Color is used to indicate the molecular density/degree of clustering from low (violet) to high (red). (d) Magnified images of individual clusters before (d1) and after (d2) heat treatment at 150 °C for 1 h. (e) Magnified images of clusters with molecules represented by crosses

before (e1) and after (e2) heat treatment at 150 °C for 1 h. (f) Size distribution of the clusters and (g) number of molecules per cluster before (f1, g1) and after (f2, g2) heat treatment at 150 °C for 1 h.

MD Simulations of Fe^{III}-Coordinated GA and TA Complexes. Using computational simulations, we further elucidated intra and intermolecular factors that may influence the observed structural sensitivity of TA/Fe^{III} (and the non-responsiveness of GA/Fe^{III}) to heat treatment. First, we used *in vacuo* density functional theory to predict temperature-dependent isomerization processes that could facilitate structural rearrangements of local Fe^{III} coordination sites. Using explicit solvent classical MD, we then investigated the influence of temperature on self-assembled aggregates of Fe^{III}-coordinated GA or TA complexes. Of note, in the absence of atomically precise details for the experimentally synthesized amorphous MPN structures, these computational models provide an atomically resolved insight and offer a fundamental rationale behind the molecular interactions and assembly mechanisms that translate to the solid-state morphology of MPN surfaces.

The microstructure and resulting properties of supramolecular metal–ligand networks is significantly affected by the stereochemistry of the component metal complexes.[31] The incorporation of isomerizable stimuli-responsive organic components (*e.g.* azobenzenes, spiropyranes) is a well-established strategy to endow photo- or thermal-switchable behavior into metal–organic materials.[32] To investigate the possibility of Fe-based isomerization processes to contribute to the observed temperature responsiveness, we investigated facial(*fac*)/meridional(*mer*) and Δ/Λ isomerization of an isolated $[Fe^{III}(GA)_3]^{3-}$ complex using density functional and wavefunction theory (see **Figure 6**, **Movies S1** and **S2**). We hypothesize that these isomerization processes could be partially responsible for the observed temperature dependency by facilitating structural rearrangements of local coordination sites within TA networks. While Δ and Λ isomers are degenerate in isolation, metal-rich regions of the network would have multiple Fe^{III} coordination complexes in close proximity. Thus, the relative stereochemistry of these complexes could impact their packing, as different cluster arrangements could have different energies (*e.g.*, ΔΔ and ΔΛ cluster pairs would be diastereomeric and not enantiomeric). By accessing different coordination isomers, adjacent Fe complexes could adopt more thermodynamically favorable configurations in response to their local environment. Both molecular and macroscopic chirality can emerge within metal–organic materials even when achiral organic ligands are used.[33] Such systems can have multidomain morphologies, with the coordination networks forming homochiral regions despite the bulk material being racemic.[33]

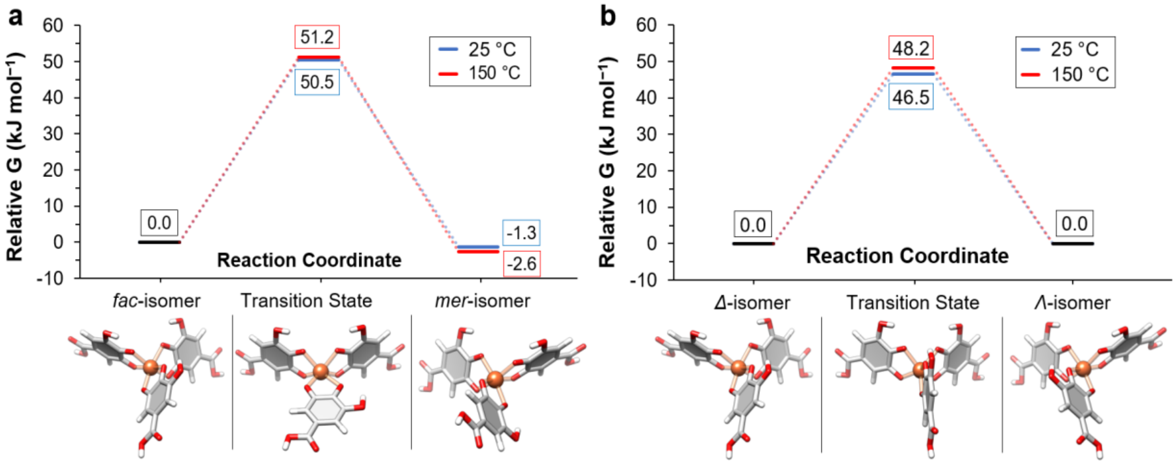

Figure 6. Potential energy surface diagrams for the isomerization of the $[Fe^{III}(GA)_3]^{3-}$ complex, calculated at 25 and 150 °C using DLPNO-CCSD(T)/aug-cc-pVTZ//B3LYP-D3(BJ)/def2-TZVP. (a, b) Optimized structures and relative Gibbs free energies for *fac*/*mer* isomerization and Δ/Λ isomerization, respectively.

As **Figure 6** indicates, the calculated barriers for both *fac*/*mer* and Δ/Λ isomerization of a prototypical $[Fe^{III}(GA)_3]^{3-}$ complex are low (<52 kJ mol^{-1}) and indicative of the occurrence of fast equilibration even at room temperature (25 °C) (**Table S1**). Although restrictions in the torsional motion of the GA subunits might slow these processes somewhat within an actual network, these calculations indicate that the underlying Fe^{III} coordination sites of the TA and GA networks are flexible when considered in isolation. As rapid equilibration would be expected at both temperatures, thermally driven structural changes can more readily be ascribed to interactions between the organic branches, which is gauged with classical all-atom MD simulations described below. However, the inherent flexibility of the Fe^{III} coordination sites would likely play a complementary role by allowing thermally driven structural rearrangements to occur within the metal-rich regions.

The equilibrium structures of three representative, Fe^{III}-coordinated GA or TA complexes ($2\times[Fe^{III}(GA)_3]^{3-}$, $20\times[Fe^{III}(GA)_3]^{3-}$, and $2\times[Fe^{III}(TA)_3]^{3-}$) were determined using MD at two different temperatures, 27 °C (300 K) and 150 °C (423 K), each replicated multiple times for statistical sampling. This was enabled through developing and validating classical MD parameters for $[Fe^{III}(GA)_3]^{3-}$ and $[Fe^{III}(TA)_3]^{3-}$ consistent/compatible with the biomolecular CHARMM family of force fields,[34,35] parameterized to reproduce the quantum mechanically (QM) optimized *fac*-Δ, galloyl–Fe^{III} octahedral coordination geometry. Comprehensive details of the procedures employed, and force field parameters are presented in the Supporting Information.

In agreement with the observed experimental characterizations, our MD simulations reveal that small GA/Fe^{III} aggregates are invariant to substantial rearrangements upon heating. We find that electrostatic repulsions between $[Fe^{III}(GA)_3]^{3-}$ complexes sterically hinder the establishment of enduring close contacts (<0.5 nm)—instead, only transient interactions are formed over the simulation trajectories (**Figure S26**). The minimum intercomplex distance between $[Fe^{III}(GA)_3]^{3-}$ complexes in **Figure 7a** also supports this temperature invariance, with the cumulative area under the probability distribution curves showing that close contacts (<0.5 nm) only occur in a negligible 4.6% (27 °C) and 2.2% (150 °C) of the respective ensemble configurations. Similarly, increasing the $[Fe^{III}(GA)_3]^{3-}$ density within the simulation cell did not result in significantly larger or more persistent aggregates/clusters at the lower temperature regime (**Figure 7b, 7c**). Although classical all-atom simulations are currently limited to modeling initial stages of metal–phenolic complex assembly and cannot comprehensively reproduce the resultant network, our results highlight how the i) short GA chains, ii) strong covalent-like catechol/galloyl–Fe^{III} coordination bonds, and iii) crowded negatively charged environment collectively limit the ability of the GA/Fe^{III} complex to modulate (π–π or hydrogen bonding) intercomplex interactions. This implies that GA/Fe^{III} MPNs have a limited capacity to structurally rearrange, even with increased kinetic energy (at 150 °C), as Fe^{III} ions act as pins to maintain the rigidity of the supramolecular network structure.

For the TA/Fe^{III} systems, the all-atom MD results likewise correlate with the experimental characterizations. The temperature increase to 150 °C led to a systematic decrease in the radius of gyration of $2\times[Fe^{III}(TA)_3]^{3-}$, accompanied by a decrease in accessible surface area, and an increase in intercomplex contact surface area between the $[Fe^{III}(TA)_3]^{3-}$ subunits (**Figures 7d, 7e** and **S27**). This indicates that a more compact TA/Fe^{III} MPN film is likely established, accompanied by the formation of hydrophobic domains. Although our simulations show that environmental temperature did not greatly influence interbranch hydrogen bonding (**Figure 7f**) or the absolute number of π–π bonds formed between phenol rings (**Figure 7g, S28**), there was a statistically significant enhancement in the number of π–π bonds involved in formation of the hydrophobic domains at 150 °C compared with that observed at 27 °C (**Figure 7g, S28**). Importantly, at the elevated temperature, aromatics interact across adjacent $[Fe^{III}(TA)_3]^{3-}$ complexes as opposed to interactions between the arms of the three TA molecules coordinating around a single Fe^{III} center observed at the lower temperature (**Figure 7h**).

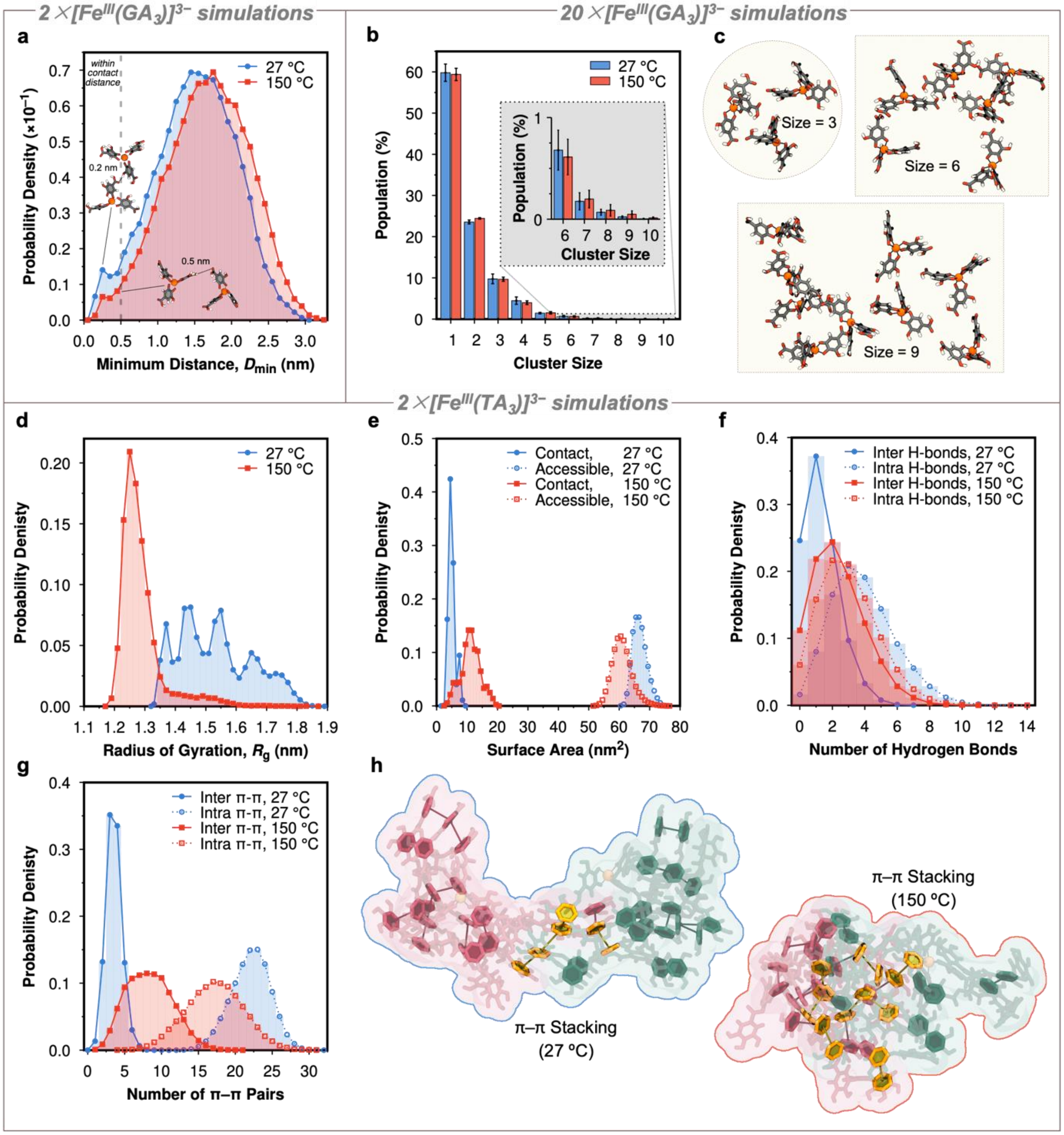

Figure 7. Statistical properties and structures extracted from equilibrated MD simulations of Fe^{III}-coordinated GA and TA complexes in solution at 27 °C (300 K) and 150 °C (423 K). (a) Probability distributions for the minimum interaction distances between two $[Fe^{III}(GA)_3]^{3-}$ complexes. Atoms

are shown in gray (C), red (O), white (H), and orange (Fe^{III}). Solvent molecules and counterions are not shown for clarity. (b) Aggregate cluster size distributions and (c) representative images from simulations of $20\times[Fe^{III}(GA)_3]^{3-}$. Error bars in (b) denote standard deviations from three replicate trajectories. (d–g) Probability distribution plots of radius of gyration (d), accessible surface area and contact surface area (e), hydrogen bonding (f), and π–π stacking interactions (g) for $2\times[Fe^{III}(TA)_3]^{3-}$. In (f) and (g), inter/intracomplex interactions between/within $[Fe^{III}(TA)_3]^{3-}$ subunits are distinguished using open/closed symbols, respectively. (h) Representative images showing the median number of π–π stacking phenol rings at each temperature. Intercomplex π–π interactions (hydrophobic domains) are highlighted in yellow.

Conclusions

We have demonstrated that metal–phenol coordination networks (in the form of capsules) exhibit elasticity and undergo heat-induced structural rearrangements depending on the conformational changes of the phenolic building blocks and flexibility of the Fe^{III} coordination center. By using single-molecule localization microscopy and theoretical molecular simulations, we showed that the thermal treatment of TA/Fe^{III} networks promotes the formation of hydrophobic domains, resulting in considerable changes in the morphology of the network. The in-depth understanding of the heat-induced structural reorganization of MPNs gained in the present work provides opportunities to design materials with tunable size, thickness, hydrophobicity, surface roughness, and wettability, which are known to influence the permeability and drug loading efficiency of MPN materials, parameters that are important to control for practical applications of such systems.

Methods

Materials. Iron(III) chloride hexahydrate ($FeCl_3 \cdot 6H_2O$), TA, GA, phosphoric acid, FITC-dextran (M_w = 20 kDa), polyethyleneimine (PEI, M_w = ~25 kDa), albumin-FITC, and NR were purchased from Sigma-Aldrich. PS particles (D = 3.3 ± 0.13 μm and 1 μm) were purchased from microParticles GmbH. Tetrahydrofuran (THF) and methanol were purchased from Chem-Supply. High-purity (Milli-Q) water with a resistivity of 18.2 MΩ cm was obtained from an inline Millipore Rios/Origin water purification system.

Characterization. UV–visible (UV–vis) absorption spectra were recorded on a Varian Cary 4000 UV–vis spectrophotometer. The morphology and size of the particles was observed by field-emission scanning electron microscopy (Quanta 200 FEI) at 10 kV. For sample preparation, a drop of the particle suspension was placed on a metallic support with carbon tape and allowed to dry prior to sputter coating with gold. EDS profiling and mapping were also performed on an FEI Quanta scanning electron microscope. AFM experiments were performed on a JPK NanoWizard II BioAFM instrument. The mechanical properties of the capsules dispersed in water were determined using a Cypher atomic force microscope (Asylum Research, Goleta, CA, USA) with contact mode cantilevers. Fluorescence spectra were recorded on a Horiba FL-322 Fluorolog-3 spectrophotometer equipped with a 450 W xenon arc lamp as excitation source. The emission spectra were recorded at different excitation wavelengths, and the emission and excitation slits were 10 nm and 5 nm, respectively. T_g was determined using a differential scanning calorimeter (PerkinElmer). The sample (3–5 mg) was loaded into aluminum pans with lids, and the heating and cooling rates were set at 10 °C min^{-1}. TGA was performed on a TG–FTIR analyzer (Netzsch) under nitrogen flow with a heating rate of 10 °C min^{-1}.

PAINT images were acquired on a Nikon N-STORM system equipped with a Nikon 100× 1.4 NA oil immersion objective. The focus and total internal reflection fluorescence imaging angle were adjusted to obtain a high signal-to-noise ratio. A 561 nm laser was used for the excitation of NR and a 488 laser was used for the excitation of albumin-FITC. All time lapses were recorded onto a 256 pixel × 256 pixel region using an electron-multiplying charge coupled device camera. For each image, 3000–6000 frames were sequentially acquired, and images were analyzed using a N-STORM software ImageJ. Confocal microscopy images were acquired using a Nikon A1R confocal microscope with a 100× 1.4NA oil immersion objective. HPLC was performed on a Shimadzu SCL-10AVP equipped with a RESTEK column model Ultra AQ C18 5 µm (150 × 4.6 mm) and a UV detector (wavelength used was 280 nm). All chromatograms were generated by LabSolution software (Shimadzu). The injection volume and flow rate were 20 µL and 1 mL min^{-1}, respectively. Gradient elution was performed using solvent A (0.5% phosphoric acid) and solvent B (methanol + 0.5% phosphoric acid). The gradient was 10% solvent B from 0–5 min, 50% solvent B from 5–10 min, 100% solvent B from 10–15 min, and 10% solvent B from 15–25 min. The amount of Fe was quantified by ICP-OES.

Preparation of TA/Fe^{III} and GA/Fe^{III} Capsules by Discrete Assembly Method. To prepare TA/Fe^{III} capsules, the PS particles (3.3 and 1 µm in diameter; 50 µL, 10% w/v) were washed with Milli-Q water (500 µL) three times. A mixture of TA solution (500 µL, 20 mM) and $FeCl_3 \cdot 6H_2O$ solution (500 µL, 30 mM) were added to Milli-Q water (1 mL), which was then centrifuged (5000 *g*, 5 min) and filtered with a 0.22 µm syringe filter. To this solution, a suspension of the PS particles (200 µL) was added. The mixture was vortexed for 10 s. The particles were then washed with Milli-Q water three times to remove unreacted TA and Fe^{III} ions by centrifuging (3000 *g*, 1 min) and resuspension in Milli-Q water. To remove the PS template and obtain capsules, the pellet was incubated with THF (1 mL) for 1 h, and centrifuged at 3000 *g* for 1 min. The supernatant was removed, and suspended in Milli-Q water, centrifuged again at 3000 *g* for 1 min and this washing process was repeated thrice.

To prepare the GA/Fe^{III} capsules, the PS particles (3.3 μm in diameter; 50 μL, 10% w/v) were added to a mixture (2 mL) of GA (18.5 mM) and $FeCl_3·6H_2O$ (15 mM), and the suspension was vortexed for 10 s and centrifuged at 3000 *g* for 1 min to remove free GA/Fe^{III} complexes. The pellet was then washed three times in Milli-Q water and resuspended in THF to dissolve PS to obtain the capsules. In particular, the pellet was incubated with THF (1 mL) for 1 h and centrifuged at 3000 *g* for 1 min. The supernatant was removed, and suspended in Milli-Q water, centrifuged again at 3000 *g* for 1 min and this washing process was repeated thrice.

Preparation of TA/Fe^{III} Films by Discrete Assembly Method. For the preparation of TA/Fe^{III} films, glass slides were used as substrates. Before coating, the substrates were cleaned with piranha solution (30% H_2O_2/98% H_2SO_4, 1:3 v/v) for 5 min, rinsed with Milli-Q water, and dried in air. The glass slides were then immersed in a PEI solution (1 mg mL^{-1}, 0.5 M NaCl) for 30 min, rinsed with Milli-Q water three times, and air dried before use.

For coating, the glass substrates were introduced into a mixture (50 mL) of TA solution (2 mg mL^{-1}) and $FeCl_3·6H_2O$ solution (1 mg mL^{-1}). The mixture with the glass substrates were left on a shaker set at 90 rpm for 24 h. The coated glass slides were then gently washed with Milli-Q three times and air dried.

Determination of Iron Content. To construct a calibration curve, standard solutions, with iron contents in the range of 1–20 ppm, were prepared in a mixture of HNO_3 and water (1:4 (v/v)). Capsule suspensions (1 mg mL^{-1}) were incubated in 1 M HNO_3 overnight to disassemble the capsules and then diluted in Milli-Q water for ICP-OES analysis.

Heat Treatment. For the heat treatment, the TA/Fe^{III} capsule and GA/Fe^{III} capsule aqueous suspensions (1 mL) were incubated in an oven at 150 ℃ for 15 or 30 min. The TA/Fe^{III}-coated glass slides were incubated at 150 ℃ for 1 h. Before AFM, PAINT, and SEM characterization, the heat-treated capsules were resuspended in water. The morphology of the capsules and coated glass substrates was studied *via* AFM and SEM, and hydrophobicity mapping was performed using PAINT before and after heat treatment.

Mechanical Studies. A fresh TA/Fe^{III}-coated PS suspension (30 µL) was dropped onto a sectioned amine-terminated glass substrate (1 cm × 1 cm) and left undisturbed for 2 h. An aliquot (30 µL) of the TA/Fe^{III}-coated PS suspension was then placed onto the glass substrate and the PS templates were removed by immersing the glass substrate with the immobilized particles in fresh THF for 2 h. The residual THF on the glass slides and capsules was removed by immersing the slides with immobilized capsules twice in water. The mechanical properties of the capsules on the glass substrates (immersed in water) before and after heat treatment at 150 °C were then measured. The measurements were performed on a Cypher atomic force microscope (Asylum Research, Goleta, CA, USA) in Milli-Q water (18.2 MΩ cm) with BioLever mini cantilevers (spring constant 0.02–0.14 N m^{-1}, Olympus, Tokyo, Japan). The spring constant of the cantilever was determined to be 0.062 N m^{-1}. The location of individual capsules was identified through AFM imaging under tapping mode. An individual capsule was then indented with the AFM tip at a specified applied force (1.5 nN) and a constant velocity (0.5 µm s^{-1}) under contact mode, and the resulting F–δ curve was recorded. The F–δ curves of five different capsules were collected and analyzed using Asylum Research software.

Hydrophobicity Tracking. MPN capsule suspensions (5 µL) before and after heat treatment were added to a microscopic glass slide for PAINT imaging. After 20 min, NR (20 µL, 10 nM) was added to the capsule suspension. PAINT images were acquired to identify changes in the hydrophobicity of the capsules following heat treatment. Similarly, TA/Fe^{III}-coated glass substrates before and after thermal treatment were imaged after the addition of NR (10 nM). The PAINT images were analyzed using the NIS Elements Nikon software. A list of localizations by Gaussian fitting fluorescent spots of the blinking dye molecules were processed by the software, which also allowed for drift correction. Blinking events that are detected in consecutive frames are counted as single molecules by the software. For each sample, between 15 and 20 capsules were analyzed. The number and size of clusters on the MPN-coated glass slides were analyzed using ImageJ, and the number of localizations per cluster were calculated using NIS Elements Nikon software; approximately 100 clusters were calculated to obtain a precise distribution of localization events per cluster.

Permeability. To examine the permeability of the untreated and heat-treated TA/Fe^{III} capsules, a capsule suspension (20 μL) was incubated with FITC-dextran (50 μL, 1 mg mL^{-1}, 20 kDa) for 10 min. The samples were imaged using confocal microscopy and capsules with dark interiors were considered impermeable and those with the same interior as background signal were considered permeable.

Loading of Albumin-FITC. To demonstrate the interaction of the TA/Fe^{III} capsules with proteins, the capsules before and after thermal treatment at 150 °C for 15 min were incubated with albumin-FITC (1 mg mL^{-1}) for 1 h. The samples were then imaged using a Nikon N-STORM microscope equipped with a 488 nm laser to estimate the binding of albumin to the capsules.

ASSOCIATED CONTENT

Supporting Information. Computational details for QM and MD simulations; SEM, AFM, differential scanning calorimetry, TGA, HPLC, FTIR, and PAINT characterization of capsules and thin films; force field parameterization of Fe^{III}–galloyl; characterization of time-evolved structural properties obtained from independent MD simulations and raw QM energies and optimized structures (PDF).

Movie S1. Fe^{III}/Gallic acid *fac*/*mer* isomerization process (AVI).

Movie S2. Fe^{III}/Gallic acid Δ/Λ isomerization process (AVI).

This material is available free of charge *via* the Internet at http://pubs.acs.org.

AUTHOR INFORMATION

Corresponding Authors

Frank Caruso – ARC Centre of Excellence in Convergent Bio-Nano Science and Technology, and the Department of Chemical Engineering, The University of Melbourne, Parkville, Victoria 3010, Australia. Email: fcaruso@unimelb.edu.au

Francesca Cavalieri – School of Science, RMIT University, Victoria 3001, Australia; Dipartimento di Scienze e Tecnologie Chimiche, Università degli Studi di Roma "Tor Vergata", via della ricerca scientifica 1, 00133, Rome, Italy. Email: francesca.cavalieri@rmit.edu.au

Irene Yarovsky – School of Engineering, RMIT University, Victoria, 3001, Australia. Email: irene.yarovsky@rmit.edu.au

Authors

Sukhvir Kaur Bhangu – ARC Centre of Excellence in Convergent Bio-Nano Science and Technology, and the Department of Chemical Engineering, The University of Melbourne, Parkville, Victoria 3010, Australia; School of Science, RMIT University, Victoria 3001, Australia

Patrick Charchar – School of Engineering, RMIT University, Victoria, 3001, Australia

Benjamin Noble – School of Engineering, RMIT University, Victoria, 3001, Australia

Chan-Jin Kim – ARC Centre of Excellence in Convergent Bio-Nano Science and Technology, and the Department of Chemical Engineering, The University of Melbourne, Parkville, Victoria 3010, Australia.

Shuaijun Pan – ARC Centre of Excellence in Convergent Bio-Nano Science and Technology, and the Department of Chemical Engineering, The University of Melbourne, Parkville, Victoria 3010, Australia.

Author Contributions

‡S.K.B. and P.C. contributed equally to this work. The manuscript was written through contributions of all authors. All authors have given approval to the final version of the manuscript.

Notes

The authors declare no competing financial interest.

ACKNOWLEDGMENT

This research was conducted and funded by the Australian Research Council (ARC) Centre of Excellence in Convergent Bio-Nano Science and Technology (project number CE140100036). F. Caruso acknowledges the award of a National Health and Medical Research Council Senior Principal Research Fellowship (GNT1135806) and F. Cavalieri acknowledges the award of an RMIT Vice Chancellor Senior Research Fellowship. I.Y. acknowledges the ARC for financial support under the Discovery Project scheme (DP170100511). This research was undertaken with the assistance of resources from the National Computational Infrastructure (NCI) (grant e87) provided by the Australian government. This work was performed in part at the Materials Characterization and Fabrication Platform (MCFP) at The University of Melbourne.

REFERENCES

1. Rahim, M. A.; Kristufek, S. L.; Pan, S.; Richardson, J. J.; Caruso, F. Phenolic Building Blocks for the Assembly of Functional Materials. *Angew. Chem., Int. Ed.* **2019**, *58*, 1904–1927.

2. Guo, J.; Ping, Y.; Ejima, H.; Alt, K.; Meissner, M.; Richardson, J. J.; Yan, Y.; Peter, K.; Von Elverfeldt, D.; Hagemeyer, C. Engineering Multifunctional Capsules through the Assembly of Metal–Phenolic Networks. *Angew. Chem., Int. Ed.* **2014**, *53,* 5546–5551.

3. Maerten, C.; Lopez, L.; Lupattelli, P.; Rydzek, G.; Pronkin, S.; Schaaf, P.; Jierry, L.; Boulmedais, F. Electrotriggered Confined Self-Assembly of Metal–Polyphenol Nanocoatings Using a Morphogenic Approach. *Chem. Mater.* **2017**, *29*, 9668–9679.

4. Ejima, H.; Richardson, J. J.; Liang, K.; Best, J. P.; van Koeverden, M. P.; Such, G. K.; Cui, J.; Caruso, F. One-Step Assembly of Coordination Complexes for Versatile Film and Particle Engineering. *Science* **2013**, *341*, 154–157.

5. Zhong, Q.-Z.; Pan, S.; Rahim, M. A.; Yun, G.; Li, J.; Ju, Y.; Lin, Z.; Han, Y.; Ma, Y.; Richardson, J. J.; Caruso, F. Spray Assembly of Metal–Phenolic Networks: Formation, Growth, and Applications. *ACS Appl. Mater. Interfaces* **2018**, *10*, 33721–33729.

6. Zhong, Q.-Z.; Li, S.; Chen, J.; Xie, K.; Pan, S.; Richardson, J. J.; Caruso, F. Oxidation-Mediated Kinetic Strategies for Engineering Metal–Phenolic Networks. *Angew. Chem., Int. Ed.* **2019**, *58*, 12563–12568.

7. Rahim, M. A.; Björnmalm, M.; Bertleff-Zieschang, N.; Besford, Q.; Mettu, S.; Suma, T.; Faria, M.; Caruso, F. Rust-Mediated Continuous Assembly of Metal–Phenolic Networks. *Adv. Mater.* **2017**, *29*, 1606717.

8. Park, J. H.; Choi, S.; Moon, H. C.; Seo, H.; Kim, J. Y.; Hong, S. P.; Lee, B. S.; Kang, E.; Lee, J.; Ryu, D. H.; Choi, I. S. Antimicrobial Spray Nanocoating of Supramolecular Fe(III)-Tannic Acid Metal-Organic Coordination Complex: Applications to Shoe Insoles and Fruits. *Sci. Rep.* **2017**, *7*, 6980.

9. Pan, S.; Guo, R.; Bertleff-Zieschang, N.; Li, S.; Besford, Q. A.; Zhong, Q.-Z.; Yun, G.; Zhang, Y.; Cavalieri, F.; Ju, Y.; Caruso, F. Modular Assembly of Host–Guest Metal–Phenolic Networks Using Macrocyclic Building Blocks. *Angew. Chem., Int. Ed.* **2020**, *59*, 275–280.

10. Yun, G.; Richardson, J. J.; Biviano, M.; Caruso, F. Tuning the Mechanical Behavior of Metal–Phenolic Networks through Building Block Composition. *ACS Appl. Mater. Interfaces* **2019**, *11*, 6404–6410.

11. Pan, S.; Goudeli, E.; Chen, J.; Lin, Z.; Zhong, Q.-Z.; Zhang, W.; Yu, H.; Guo, R.; Richardson, J. J.; Caruso, F. Exploiting Supramolecular Dynamics in Metal–Phenolic Networks to Generate Metal–Oxide and Metal–Carbon Networks. *Angew. Chem., Int. Ed.* **2021**, *60*, 14586–14594.

12. Chen, J.; Pan, S.; Zhou, J.; Zhong, Q.-Z.; Qu, Y.; Richardson, J. J.; Caruso, F. Programmable Permeability of Metal–Phenolic Network Microcapsules. *Chem. Mater.* **2020**, *32*, 6975–6982.

13. Glinel, K.; Sukhorukov, G. B.; Möhwald, H.; Khrenov, V.; Tauer, K. Thermosensitive Hollow Capsules Based on Thermoresponsive Polyelectrolytes. *Macromol. Chem. Phys.* **2003**, *204*, 1784–1790.

14. Trushina, D. B.; Bukreeva, T. V.; Borodina, T. N.; Belova, D. D.; Belyakov, S.; Antipina, M. N. Heat-Driven Size Reduction of Biodegradable Polyelectrolyte Multilayer Hollow Capsules Assembled on $CaCO_3$ Template. *Colloids Surf., B* **2018**, *170*, 312–321.

15. Köhler, K.; Shchukin, D. G.; Sukhorukov, G. B.; Möhwald, H. Drastic Morphological Modification of Polyelectrolyte Microcapsules Induced by High Temperature. *Macromolecules* **2004**, *37*, 9546–9550.

16. Leporatti, S.; Gao, C.; Voigt, A.; Donath, E.; Mohwald, H. Shrinking of Ultrathin Polyelectrolyte Multilayer Capsules Upon Annealing: A Confocal Laser Scanning Microscopy and Scanning Force Microscopy Study. *Eur. Phys. J. E: Soft Matter Biol. Phys.* **2001**, *5*, 13–20.

17. Yan, Y.; Huang, J.; Tang, B. Z. Kinetic Trapping – A Strategy for Directing the Self-Assembly of Unique Functional Nanostructures. *Chem. Commun.* **2016**, *52*, 11870–11884.

18. Rahim, M. A.; Kempe, K.; Müllner, M.; Ejima, H.; Ju, Y.; van Koeverden, M. P.; Suma, T.; Braunger, J. A.; Leeming, M. G.; Abrahams, B. F.; Caruso, F. Surface-Confined Amorphous Films from Metal-Coordinated Simple Phenolic Ligands. *Chem. Mater.* **2015**, *27*, 5825–5832.

19. Zou, Y.; Guo, J.; Yin, S. W.; Wang, J. M.; Yang, X. Q. Pickering Emulsion Gels Prepared by Hydrogen-Bonded Zein/Tannic Acid Complex Colloidal Particles. *J. Agric. Food Chem.* **2015**, *63*, 7405–7414.

20. Wang, Y.; Gao, X.; Xiao, Y.; Zhao, Q.; Yang, J.; Yan, Y.; Huang, J. Temperature Dependent Coordinating Self-Assembly. *Soft Matter* **2015**, *11*, 2806–2811.

21. Sharonov, A.; Hochstrasser, R. M. Wide-Field Subdiffraction Imaging by Accumulated Binding of Diffusing Probes. *Proc. Natl. Acad. Sci. U. S. A.* **2006**, *103*, 18911–18916.

22. Bongiovanni, M. N.; Godet, J.; Horrocks, M. H.; Tosatto, L.; Carr, A. R.; Wirthensohn, D. C.; Ranasinghe, R. T.; Lee, J. E.; Ponjavic, A.; Fritz, J. V.; Dobson, C. M.; Klenerman, D.; Lee, S. F. Multi-Dimensional Super-Resolution Imaging Enables Surface Hydrophobicity Mapping. *Nat. Commun.* **2016**, *7*, 13544.

23. Sackett, D. L.; Wolff, J. Nile Red as a Polarity-Sensitive Fluorescent Probe of Hydrophobic Protein Surfaces. *Anal. Biochem.* **1987**, *167*, 228–234.

24. Diaz, G.; Melis, M.; Batetta, B.; Angius, F.; Falchi, A. M. Hydrophobic Characterization of Intracellular Lipids *in Situ* by Nile Red Red/Yellow Emission Ratio. *Micron* **2008**, *39*, 819–824.

25. Gahlmann, A.; Ptacin, J. L.; Grover, G.; Quirin, S.; von Diezmann, L.; Lee, M. K.; Backlund, M. P.; Shapiro, L.; Piestun, R.; Moerner, W. E. Quantitative Multicolor Subdiffraction Imaging of Bacterial Protein Ultrastructures in Three Dimensions. *Nano Lett.* **2013**, *13*, 987–993.

26. Kucherak, O. A.; Oncul, S.; Darwich, Z.; Yushchenko, D. A.; Arntz, Y.; Didier, P.; Mely, Y.; Klymchenko, A. S. Switchable Nile Red-Based Probe for Cholesterol and Lipid Order at the Outer Leaflet of Biomembranes. *J. Am. Chem. Soc.* **2010**, *132*, 4907–4916.

27. Schellman, J. A. Temperature, Stability, and the Hydrophobic Interaction. *Biophys. J.* **1997**, *73*, 2960–2964.

28. Kasprzak, M. M.; Erxleben, A.; Ochocki, J. Properties and Applications of Flavonoid Metal Complexes. *RSC Adv.* **2015**, *5*, 45853–45877.

29. Gruβmayer, K. S.; Yserentant, K.; Herten, D. P. Photons In - Numbers Out: Perspectives in Quantitative Fluorescence Microscopy for *in Situ* Protein Counting. *Methods Appl. Fluoresc.* **2019**, *7*, 012003.

30. Das, R. P.; Singh, B. G.; Kunwar, A.; Ramani, M. V.; Subbaraju, G. V.; Hassan, P. A.; Priyadarsini, K. I. Tuning the Binding, Release and Cytotoxicity of Hydrophobic Drug by Bovine Serum Albumin Nanoparticles: Influence of Particle Size. *Colloids Surf., B* **2017**, *158*, 682–688.

31. Wang, S.; Dormidontova, E. E. Tunable Supramolecular Networks *via Cis-Trans* Metal–Ligand Isomerization. *Soft Matter* **2010**, *6*, 1004–1014.

32. Castellanos, S.; Kapteijn, F.; Gascon, J. Photoswitchable Metal Organic Frameworks: Turn on the Lights and Close the Windows. *CrystEngComm* **2016**, *18*, 4006–4012.

33. di Gregorio, M. C.; Shimon, L. J. W.; Brumfeld, V.; Houben, L.; Lahav, M.; van der Boom, M. E. Emergence of Chirality and Structural Complexity in Single Crystals at the Molecular and Morphological Levels. *Nat. Commun.* **2020**, *11*, 380.

34. Mackerell, A. D.; Feig, M.; Brooks, C. L. Extending the Treatment of Backbone Energetics in Protein Force Fields: Limitations of Gas-Phase Quantum Mechanics in Reproducing Protein Conformational Distributions in Molecular Dynamics Simulations. *J. Comput. Chem.* **2004**, *25*, 1400–1415.

35. MacKerell, A. D.; Bashford, D.; Bellott, M.; Dunbrack, R. L.; Evanseck, J. D.; Field, M. J.; Fischer, S.; Gao, J.; Guo, H.; Ha, S.; Joseph-McCarthy, D.; Kuchnir, L.; Kuczera, K.; Lau, F.

T. K.; Mattos, C.; Michnick, S.; Ngo, T.; Nguyen, D. T.; Prodhom, B.; Reiher, W. E., III *et al.* All-Atom Empirical Potential for Molecular Modeling and Dynamics Studies of Proteins. *J. Phys. Chem. B* **1998**, *102*, 3586–3616.

Table of Content Graphic